EES Batteries

PAPER

View Article Online
View Journal | View Issue



Cite this: *EES Batteries*, 2026, **2**, 270

# Synergy of organoiodide additives and co-solvent enabling high-performance wide-temperature Zn metal batteries

Xin Miao,†[a] Jingjing Bao,†[a] Shuang Li,†[a] Changjun He,[a] Ziyang Guo *[a] and Yonggang Wang *[a,b]

Although Zn metal batteries (ZMBs) are promising next-generation energy storage systems due to their high safety and low cost, serious parasitic reactions and a narrow operating-temperature range derived from aqueous electrolytes hinder their development. Herein, an optimized tetrahydrofuran (THF)/$H_2O$ (volume ratio: 50 : 50) hybrid electrolyte with a triethyl sulfonium iodide (TSI) additive (T50 + TSI) is developed for ZMBs. Incorporation of THF reconfigures the hydrogen-bonding network between water molecules, reducing the freezing point of T50 + TSI. Additionally, the synergy of organoiodide and THF optimizes the solvated $Zn^{2+}$ structure and facilitates the desolvation kinetics, realizing uniform Zn deposition, lowering Zn plating/stripping overpotentials and inhibiting $H_2$ evolution/Zn corrosion. Consequently, T50 + TSI-based Zn//Zn cells achieve a low polarization voltage of 92 mV at 2 mA $cm^{-2}$ over 7100 hours at room temperature, normally operate even at −50 °C, and stably cycle over 6400 hours at −30 °C. As a result, the Zn//NVO ($NaV_3O_8{\cdot}1.5H_2O$) batteries with T50 + TSI display stable voltage curves for 1500 cycles at 1 A $g^{-1}$. With an ultra-high loading of 15.3 mg $cm^{-2}$, the NVO cathode in T50 + TSI still exhibits a large capacity (264.0 mAh $g^{-1}$) at 0.1 A $g^{-1}$. Surprisingly, the T50 + TSI-based Zn//NVO batteries present long-term stability over 1480 cycles even at an extreme temperature of −30 °C.

Received 1st September 2025,
Accepted 16th November 2025

DOI: 10.1039/d5eb00158g

rsc.li/EESBatteries



**Broader context**

Aqueous zinc metal batteries (ZMBs) emerge as the prime candidates for large-scale energy storage, attributed to their economic viability, substantially heightened safety features and substantial theoretical energy density. Nevertheless, the serious hydrogen evolution/Zn corrosion and narrow operational temperature range derived from active $H_2O$ molecules in aqueous electrolytes critically limit the application of ZMBs. Although adding functional organic solvents into aqueous electrolytes is considered as one of the most effective methods to address the above problems, this co-solvent strategy often greatly increases the overpotentials of Zn plating/stripping behaviors and also usually proves insufficient in addressing the complex issue of dendrite formation. Here, we design a tetrahydrofuran (THF)/$H_2O$ hybrid electrolyte incorporating a triethyl sulfonium iodide (TSI) additive for ZMBs. The synergistic effects between THF and TSI effectively suppress $H_2$ evolution and corrosion on Zn anodes, lower the freezing point of the hybrid electrolyte, reduce the voltage hysteresis by accelerating the reaction kinetics of Zn deposition/dissolution and generate a robust anode interface to inhibit Zn dendrites. As a result, Zn-based cells with this hybrid electrolyte show superior performances even in a wide temperature range. This work highlights the synergistic role of solvent engineering and additive modification in advanced ZMBs.

## Introduction

Aqueous zinc metal batteries (ZMBs) should be the optimal candidates for large-scale energy storage systems, owing to their cost-effectiveness, obviously enhanced safety, and large theoretical capacity (820 mAh $g^{-1}$) and the low theoretical electrochemical potential (0.76 V *versus* the standard hydrogen electrode) of metallic Zn anodes.[1–3] Although many advantages of ZMBs relate to their high-performance Zn anodes and non-flammable aqueous electrolytes, the excessive dendrite growth, serious hydrogen evolution and anode corrosion reactions derived from highly active $H_2O$ and metallic Zn also negatively affect the cycling stability of ZMBs.[4–7] Moreover, a large number of hydrogen bonding networks between water molecules also make the freezing point of the electrolytes usually at around 0 °C, greatly limiting the potential applications of ZMBs in the cold environment.[8–11]

To tackle the above challenges presented, numerous researchers have introduced innovative concepts encompassing the employment of artificial interface architectures, modu-

[a]*College of Energy Material and Chemistry, College of Chemistry and Chemical Engineering, Inner Mongolia University, Hohhot, China. E-mail: zyguo@imu.edu.cn*
[b]*Department of Chemistry and Shanghai Key Laboratory of Molecular Catalysis and Innovative Materials, Institute of New Energy, iChEM (Collaborative Innovation Center of Chemistry for Energy Materials), Fudan University, Shanghai, China. E-mail: ygwang@fudan.edu.cn*
†These authors contributed equally to this work.

lation of electrolyte solvation structures, utilization of deep eutectic solvents, implementation of high-concentration "water-in-salt" electrolytes and so on.[12–15] Among them, adding polar organic solvents to an aqueous solution is considered a simple and economically feasible scheme to optimize ZMB electrolytes.[16–19] In general, $H_2O$ molecules, which take part in the solvated shell around $Zn^{2+}$ ions, are highly active. When functional organic solvents are introduced into aqueous electrolytes, water molecules interacting with $Zn^{2+}$ can be partly replaced with organic solvent molecules due to their larger binding capacity with $Zn^{2+}$ and thus greatly reduce the activity of $H_2O$. As a result, the introduction of functional organic solvents can greatly inhibit the highly active $H_2O$-induced $H_2$ evolution reaction (HER) and metallic Zn corrosion.[20–24] In addition, the hydrogen bonding networks of the original aqueous solution are also broken through the addition of organic solvent molecules and thus greatly lower the freezing point of the composite electrolytes, which enables ZMBs to realize long-term operation at cold temperatures much lower than 0 °C.[25–28] Nevertheless, the strong interaction between organic solvent molecules and $Zn^{2+}$ is also a double-edged sword that greatly increases the energy barrier for the desolvation process and thus significantly impedes the reaction kinetics over Zn deposition/dissolution processes.[29,30] Moreover, the mere inclusion of organic solvents into the aqueous electrolytes falls short in adequately tackling the intricate challenge of dendritic Zn formation. Hence, designing novel electrolytes with a wide operating temperature window, as well as the ability to inhibit dendrite formation, $H_2$ evolution and Zn corrosion, is still extremely important for the development of ZMBs.[31,32]

In this work, we mixed tetrahydrofuran (THF) solvent with water and further added a small quantity of triethyl sulfonium iodide (TSI) as a multi-functional additive to construct high-performance hybrid electrolytes for ZMBs. The addition of THF solvent can effectively optimize the shell structure of $Zn^{2+}$ by replacing $H_2O$ positions to inhibit the highly active $H_2O$-induced HER and metallic Zn corrosion. In addition, THF introduction can also break the hydrogen bonds between water molecules and thus expand the operation temperature range of this hybrid electrolyte by reducing its freezing point. Furthermore, $I^-$ species in organoiodide additives greatly lower the energy barrier for Zn desolvation and also induce uniform Zn deposition to inhibit dendritic formation and accelerate the Zn plating/stripping reaction kinetics on Zn anodes. More interestingly, the organic functional groups of TSI are converted into a robust and uniform solid electrolyte interface (SEI) layer on anodes to reduce the side reactions and electrode dimensional variation over cycling. As a result, Zn//Zn symmetric cells with this hybrid electrolyte display good properties at temperatures ranging from 60 to −50 °C. Furthermore, Zn//NVO full cells show excellent performance, including good rate performance and long-term cycling stability. More importantly, the Zn//NVO system even stably runs at a low temperature of −30 °C and the corresponding pouch batteries also provide power for long-term operation.

# Results and discussion

### Characterization of THF/$H_2O$-based hybrid electrolytes

The THF/$H_2O$-based solution is prepared by adding a zinc trifluoromethanesulfonate ($Zn(OTF)_2$) salt into a mixture of THF and $H_2O$ with different ratios (the volume ratios of THF/(THF + $H_2O$) are 0, 25, 50, 75 and 95%; the corresponding hybrid electrolytes are designated as T0, T25, T50, T75 and T95, respectively). To clarify the interactions between the Zn salt and solvent molecules, nuclear magnetic resonance (NMR), Fourier transform infrared (FT-IR) and Raman spectra are conducted. $^1H$ NMR spectra in Fig. 1a show that the chemical shift of H atoms in $H_2O$ for hybrid electrolytes migrates to a lower field with an increase of THF. It is well known that the position of $^1H$ in water molecules downshifts with the decrease of its surrounding electron cloud. The above phenomenon suggests that there is a higher hydrogen bonding (HB) energy of $H_2O$-THF compared with that of $H_2O$–$H_2O$, which reduces the electron density of $^1H$ in $H_2O$ and thus inhibits the HBs between water molecules. Moreover, the decreased electron density of $^1H$ in $H_2O$ is also not conducive to the formation of $Zn(H_2O)_6^{2+}$, which reduces water activity. In the FT-IR spectra (Fig. 1b), there is a wide band at around 3250 to 3500 $cm^{-1}$ assigned to the O–H stretching vibration of water in all these hybrid electrolytes, which shows a gradual blue shift as the content of the THF solvent increases. This indicates that the introduction of THF functions as an effective HB acceptor, which can bond with the $H_2O$ molecule and significantly diminish the reactivity of free water within the electrolyte system. Additionally, the incorporation of THF as a partial replacement for water in the $Zn^{2+}$ solvation structure enhances the bonding interaction between the trifluoromethanesulfonate anion and zinc cation, leading to a redshift in the vibrational frequency of the $V_{\text{asymmetric stretching}}$ (as) ($SO_3$) peak within the range of 1100 to 1300 $cm^{-1}$ (Fig. S1). Raman analysis reveals discernible peaks within the spectral range of 3200 to 3800 $cm^{-1}$, corresponding to the O–H stretching vibrations of water molecules, which are subsequently classified into three distinct categories: strong, weak, and non-hydrogen interactions (Fig. 1c, d and S2). When the THF content increases in hybrid electrolytes, a gradual increase in the proportion of non-hydrogen bonds is observed from 13.6% to 42.0%, while the proportion of strong hydrogen bonds decreases in a similar manner from 44.8% to 12.5%, indicating that THF weakens hydrogen bonds between $H_2O$ molecules and reduces the freezing point of hybrid electrolytes.[33,34]

To further clarify the reliability of the above hybrid electrolytes, the discharge/charge overpotentials of the Zn-based symmetric cells using THF/$H_2O$-based electrolytes are tested (Fig. 1e and f). As shown in Fig. 1e and f, the discharge/charge hysteresis of the symmetric batteries rises from 70 to 424 mV with the THF content increasing from 0 to 95%, which is attributed to the strong interaction of THF with $Zn^{2+}$ that results in a challenging desolvation process with $Zn^{2+}$. The ion conductivities of these hybrid electrolytes are also studied at room temperature (Fig. 1f). As shown in Fig. 1f, the ion con-

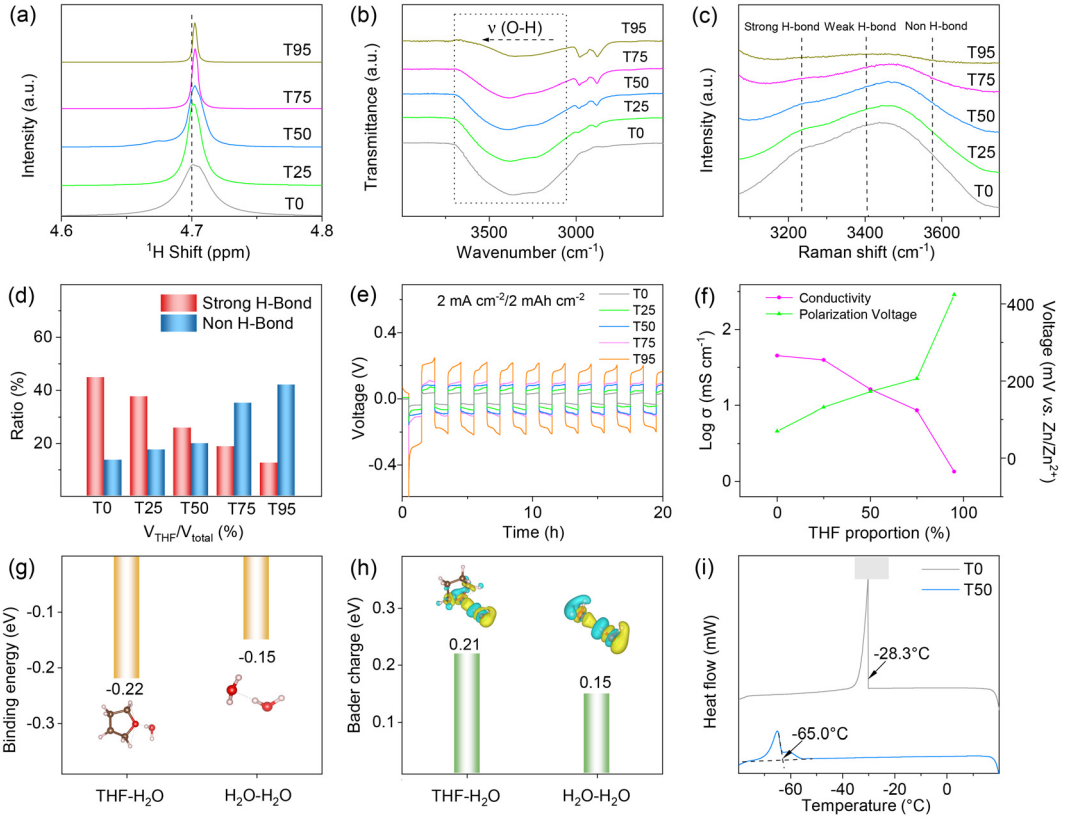


**Fig. 1** Characterization of THF/$H_2O$-based hybrid electrolytes: (a) $^1$H NMR spectra, (b) FT-IR spectra and (c) Raman spectra. (d) Ratios for the strong H-bond and non-H-bond derived from the Raman spectra of different THF/$H_2O$-based hybrid electrolytes. (e) Charge/discharge profiles of the symmetric Zn//Zn cells using T0, T25, T50, T75 or T95 at 2.0 mA cm$^{-2}$ with a limited areal capacity of 2.0 mAh cm$^{-2}$. (f) Ionic conductivities and polarization voltages of the hybrid electrolytes with different proportions of THF. (g) Binding energy and (h) Bader charge of the THF–$H_2O$ and $H_2O$–$H_2O$ electrolyte systems. (i) DSC curves for T0 and T50.

ductivities of these mixed electrolytes exhibit a declining trend with an increase in THF content, decreasing from 41.13 to 1.12 mS cm$^{-1}$ when the THF content increases from 0 to 95%, due to the low dielectric constant of the THF solvent, which reduces the conductivity of the mixed electrolytes.[35] In addition, the Zn//Ti half cells using these hybrid electrolytes are constructed and their coulombic efficiencies (CEs) are studied (Fig. S3). Among all these THF/$H_2O$ based electrolytes, the T50 based Zn//Ti half-cell shows the highest CE (~99%) for 500 cycles. Through a comprehensive consideration of the ionic conductivity and polarization voltage, T50 is considered as the optimal electrolyte.

The effects of the ultra-low temperature on these hybrid electrolytes are also analyzed (Fig. S4). After resting at −50 °C for 4 h, T50 retains its liquid state, whereas other electrolytes exhibit obvious crystallization or coagulation. Subsequently, a sequence of theoretical analyses is undertaken to gain insights into the variations of THF–$H_2O$ and $H_2O$–$H_2O$ systems (Fig. 1g and h). As shown in Fig. 1g, the binding energy between THF and $H_2O$ molecules is −0.22 eV, which is higher than that between $H_2O$ and $H_2O$ molecules (−0.15 eV). Fig. 1h also presents that the Bader charge between THF and $H_2O$ molecules (0.21 eV) is also larger than that between $H_2O$ and $H_2O$ molecules (0.15 eV). These data further demonstrate that the addition of THF molecules can bind with $H_2O$ molecules and thus effectively disrupt the original hydrogen-bonding network between $H_2O$ molecules, ultimately inducing the significant freezing-point drop of the $H_2O$/THF electrolyte system. To further evaluate the detailed solidifying point of the optimized electrolyte, the differential scanning calorimetry (DSC) curves of T50 and T0 are investigated (Fig. 1i). The freezing point of the T50 electrolyte is only −65.0 °C, which is considerably lower than the freezing point of T0 (−28.3 °C). Additionally, the ionic conductivities of T50 and T0 at different temperatures are measured (Fig. S5). When the operating temperature is above −20 °C, T0 shows higher ionic conductivities than T50. However, when the working temperature drops below −40 °C, T0 becomes the solid phase and shows low ionic conductivity because of the higher freezing point, while T50 remains in the liquid state and exhibits high ionic conductivities due to the lower freezing point. Notably, even at −65 °C, T50 still delivers a considerable ionic conductivity of 0.95 mS cm$^{-1}$, demonstrating its outstanding low-temperature performance.

It is well known that the I-based additive is beneficial for regulating the uniform Zn deposition and decreasing the $Zn^{2+}$

desolvation energy, while the organic additives are also confirmed to usually form a uniform coating layer with good mechanical toughness, effectively inhibiting the Zn electrode volume variation and corrosion of the Zn anode.[10,36] Therefore, triethyl sulfonium iodide (TSI) is introduced as an organoiodide additive into the above T50. Specifically, 25 mM, 50 mM, 100 mM and 200 mM TSI are added to T50 to form a series of TSI-based hybrid electrolytes (named T50 + *X*-TSI, *X* = 25, 50, 100, and 200). Fig. S6 shows the discharge/charge profiles of the T50 + *X*-TSI based Zn//Zn symmetric cells. It can be observed that the T50 + 50-TSI-based battery shows the lowest average discharge/charge overpotentials of 62 mV among these cells (T50 + 50-TSI is selected as the optimized sample and abbreviated as T50 + TSI in the following text).

### Electrochemical properties of T0, T50, and T50 + TSI

To analyze the corrosion effects of THF/$H_2O$ based electrolytes on Zn anodes, Tafel tests of the Zn//Zn cells using T50 + TSI, T50 and T0 are conducted (Fig. 2a). As shown in Fig. 2a, the linear polarization data of T50 + TSI present a corrosion potential of 15 mV, which is much more positive than those of T50 (7 mV) and T0 (−1 mV), while its corrosion current (0.07 mA $cm^{-2}$) is lower compared to those of T50 (0.25 mA $cm^{-2}$) and T0 (0.58 mA $cm^{-2}$). These results suggest that the synergistic effect of THF and TSI can effectively inhibit the activity of free water molecules and build a robust SEI to prevent the occurrence of Zn corrosion. The chronoamperometric (CA) profiles of the THF/$H_2O$-based cells are also tested (Fig. 2b). Fig. 2b shows that constant three-dimensional (3D) diffusion dominates in the T50 + TSI based battery, while two-dimensional (2D) diffusion with a continuous current increase seems to be the main process in T50 or T0 based cells, further confirming that TSI can greatly adjust the even distribution of a surface electric field and prevent the formation of dendrites on Zn anodes. In addition, to evaluate the HER on Zn electrodes in three electrolytes, the linear scanning voltammetry (LSV) curves in the three-electrode system with a platinum sheet as the counter electrode and Ag/AgCl as the reference electrode are studied (Fig. 2c). The T50 + TSI system shows the most negative onset potential (−1.40 V) for the HER among the three systems, suggesting that a combination of THF and TSI can obviously suppress the activity of water. To further clarify the interfacial condition of Zn anodes, cyclic voltammetry (CV) curves of the symmetric batteries using T50 + TSI, T50, or T0 are investigated (Fig. 2d and S7). It can be calculated from Fig. S7 that the electric double layer (EDL) capacitance (0.66 mF $cm^{-2}$) of T50 + TSI is significantly higher than those of T50 (0.023 mF $cm^{-2}$) and T0 (0.18 mF $cm^{-2}$), which are beneficial for mitigating the corrosion of the zinc metal, inhibiting the HER and regulating the deposition of metallic Zn.

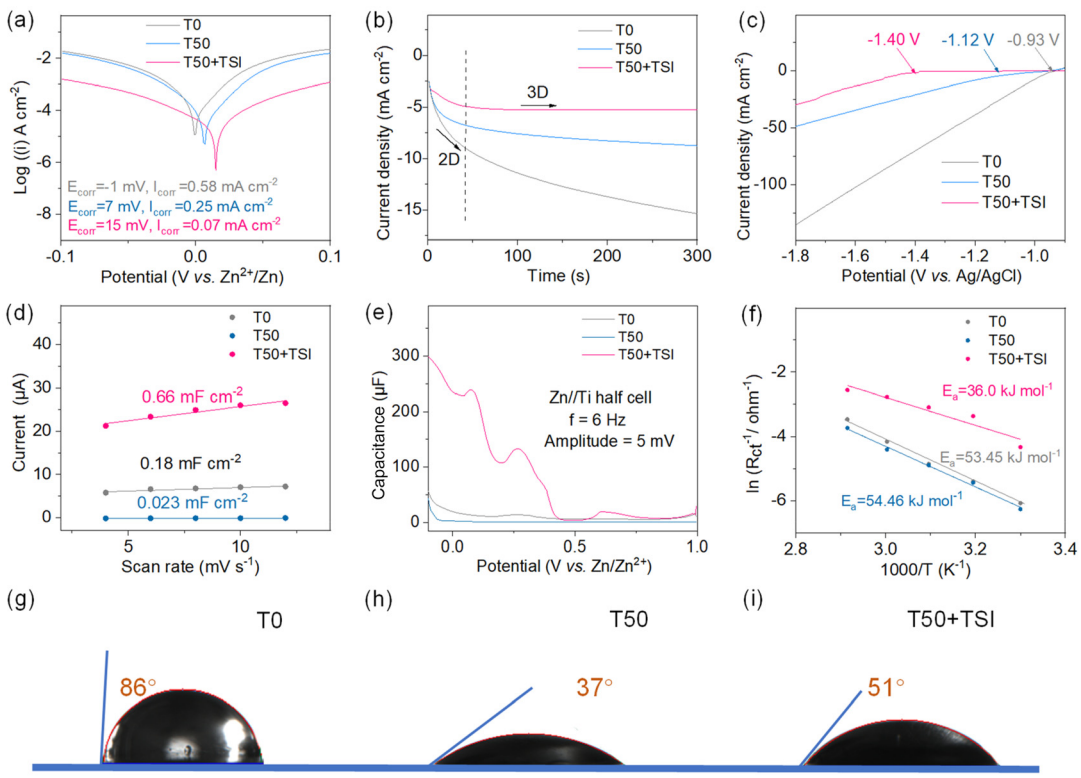


**Fig. 2** Electrochemical properties of T0, T50, and T50 + TSI. (a) Tafel plots at 0.1 mV $s^{-1}$ and (b) CA curves at a fixed overpotential of −150 mV of the Zn//Zn cells using T0, T50 or T50 + TSI. (c) HER curves of three-electrode systems with T0, T50 or T50 + TSI at a scan rate of 1 mV $s^{-1}$. (d) EDL capacitances of the Zn//Zn cells using T0, T50 or T50 + TSI. (e) ACV measurement of the Zn//Ti cells in T0, T50 or T50 + TSI. (f) $Zn^{2+}$ desolvation energy of the Zn//Zn cells in T0, T50 or T50 + TSI. (g–i) Contact angle measurements on Zn foils with (g) T0, (h) T50 or (i) T50 + TSI.

Subsequently, alternating current voltammetry (ACV) data in Fig. 2e further confirm that T50 + TSI exhibits a higher capacitance compared to T0 or T50.

The desolvation energy of $Zn^{2+}$ in different electrolytes is based on their electrochemical impedance spectrum (EIS) curves obtained at temperatures between 30 and 70 °C (Fig. 2f and S8). It can be found that the desolvation energy of $Zn^{2+}$ in T50 + TSI is 36.0 kJ $mol^{-1}$, which is much lower compared with T50 (54.46 kJ $mol^{-1}$) and T0 (53.45 kJ $mol^{-1}$). This phenomenon indicates that TSI can markedly enhance the reaction kinetics of Zn depositing/stripping. The interfacial wetting properties of the electrolytes towards Zn anodes significantly influence the nucleation dynamics of metallic Zn. To gain insights into this phenomenon, the drop contact angle methodology is employed to systematically investigate the wettability characteristics of the above electrolytes with respect to Zn foil (Fig. 2g–i). The Zn foil presents an ultra-high contact angle of 86° in T0. When 50% THF is introduced, the Zn electrode displays a relatively low contact angle of 37° in T50, suggesting that THF exhibits better wettability compared with bare water and thus can be preferentially adsorbed on the Zn surface to greatly suppress the HER and corrosion caused by active $H_2O$. The addition of TSI results in a slight increase of the contact angle (51°) between the Zn anode and T50 + TSI. This is attributed to the $TS^+$ species derived from the dissociation of TSI adsorbed on the surface of zinc anodes. The steric effect of the $TS^+$ dendritic structure that is composed of three ethyl groups prevents water molecules from coming in contact with the Zn anode, which can effectively avoid unnecessary side reactions. To further validate the above discussion, we examined the contact angles between pure water and Zn plates that were pre-treated with T50, T50 + TSI, or T50 + ZnI. The contact angle between $H_2O$ and Zn plates pre-treated with T50 is 57° (Fig. S9). After pre-treatment with T50 + ZnI, the contact angle of $H_2O$ and the zinc plate decreases to 44° due to the reduction of the interfacial free energy caused by $I^-$. The hydrophobic tendency of the zinc plate pre-immersed with T50 + TSI increases to 68°. This indicates that $TS^+$ molecules form a hydrophobic layer on the surface of Zn metal, effectively preventing the contact between active water molecules and Zn anodes.[37,38]

### Analysis and characterization of Zn anodes in T0 or T50 + TSI

To further investigate the adsorption behavior of different species on the Zn anode surface, we analyze the molecular orbital energy levels of $TS^+$, $H_2O$, THF and $OTF^-$. As shown in Fig. 3a, the lowest unoccupied molecular orbital (LUMO) energy level of $TS^+$ is −0.11 eV, which is significantly lower than those of THF (1.26 eV), $H_2O$ (1.09 eV), and $OTF^-$ (2.20 eV). This indicates that $TS^+$ is more likely to adsorb on the Zn surface when accepting electrons. In addition, the energy gaps between the LUMO and the highest occupied molecular orbital (HOMO) of $TS^+$ and THF are 8.71 eV and 8.10 eV, respectively, which are much smaller than that of $H_2O$ (9.75 eV). This suggests that after electron adsorption, it is easier for electrons to transfer from THF and $TS^+$ to the Zn surface than from $H_2O$ to the Zn anode.[39] Subsequently, *in situ* differential electrochemical mass spectrometry (DEMS) tests are applied to elucidate the generated $H_2$ conditions during cycling for the symmetric cells with T0 or T50 + TSI (Fig. 3b). It should be noted that the discharge/charge overpotentials of the Zn//Zn symmetric cell using T50 + TSI for the *in situ* DEMS test are much lower than those using T0 (Fig. S10). In addition, the amount (613 mmol) of $H_2$ generated in the T0 system significantly exceeds that in the T50 + TSI system (320 mmol). These results confirm that T50 + TSI suppresses hydrogen evolution within the battery. To further evaluate the interfacial stability, the *in situ* EIS results of Zn//Zn symmetric cells using T0 or T50 + TSI were analyzed (Fig. 3c, d and Table S1). The charge transfer resistance ($R_{ct}$) of the T0-based symmetric cell decreases dramatically from 471.0 Ω to 236.2 Ω over the Zn deposition process (Fig. 3c), suggesting the uneven Zn deposition layer and continuous variation of active reaction sites. In contrast, the cell with T50 + TSI maintains a relatively stable $R_{ct}$ value, which only slightly decreases from 77.1 Ω to 68.6 Ω during the discharge process (Fig. 3d). These results further confirm that the combination of THF and TSI effectively optimizes and stabilizes the anode interface during Zn deposition.[40–43]

To clarify the interfacial variation of Zn anodes in the symmetric batteries based on T50 + TSI and T0 over the Zn plating/stripping process, *in situ* Raman tests were performed (Fig. 3e, f and S11). Without the TSI additive, no stable anionic-absorbed interface layer was formed on the surface of the Zn anode in the T0 system over the discharge/charge process, and thus the intensity of the $\nu$(O–H) stretching vibration in the Raman spectra of the symmetric cell using T0 is strong and almost unchanged over the whole process (Fig. 3e and S11d). In the T50 + TSI system, the continuous weakening intensity of the $\nu$(O–H) stretching vibration mode is observed at the interface of the Zn anode during the discharge (or Zn deposition) process (Fig. 3f and S11c). This result indicates that the introduction of the TSI additive can induce the formation of the stable anion-absorbed interfacial layer on the Zn anodes under the influence of the inner electric field and thus decrease the amounts of active $H_2O$ molecules at the anode surface. During the subsequent charge (or Zn stripping) process, the intensity of the $\nu$(O–H) stretching vibration in Raman spectra shows minor variations, confirming that the above-formed interface layer is stable and effectively shields the anode from the active $H_2O$ molecules over the following cycles. The deposition behaviour of Zn electrodes is also monitored through an *in situ* optical microscope (Fig. 3g). As illustrated in Fig. 3g, obvious dendrites are formed on the Zn anode surface in T0 and the electrode dimensional variation is extremely apparent during the Zn plating process. In contrast, a uniform and flat coating layer forms on the Zn surface in T50 + TSI, with the electrode thickness remaining nearly constant. This suggests that T50 + TSI effectively inhibits dendritic growth and anode volume variation. Consequently, severe HER, Zn corrosion, and dendrite growth occur at the Zn anode in T0 (Fig. S12). In T50 + TSI, THF participates in the solvation structure, inhibiting the related side reactions. The adsorption of a large amount of $I^-$,

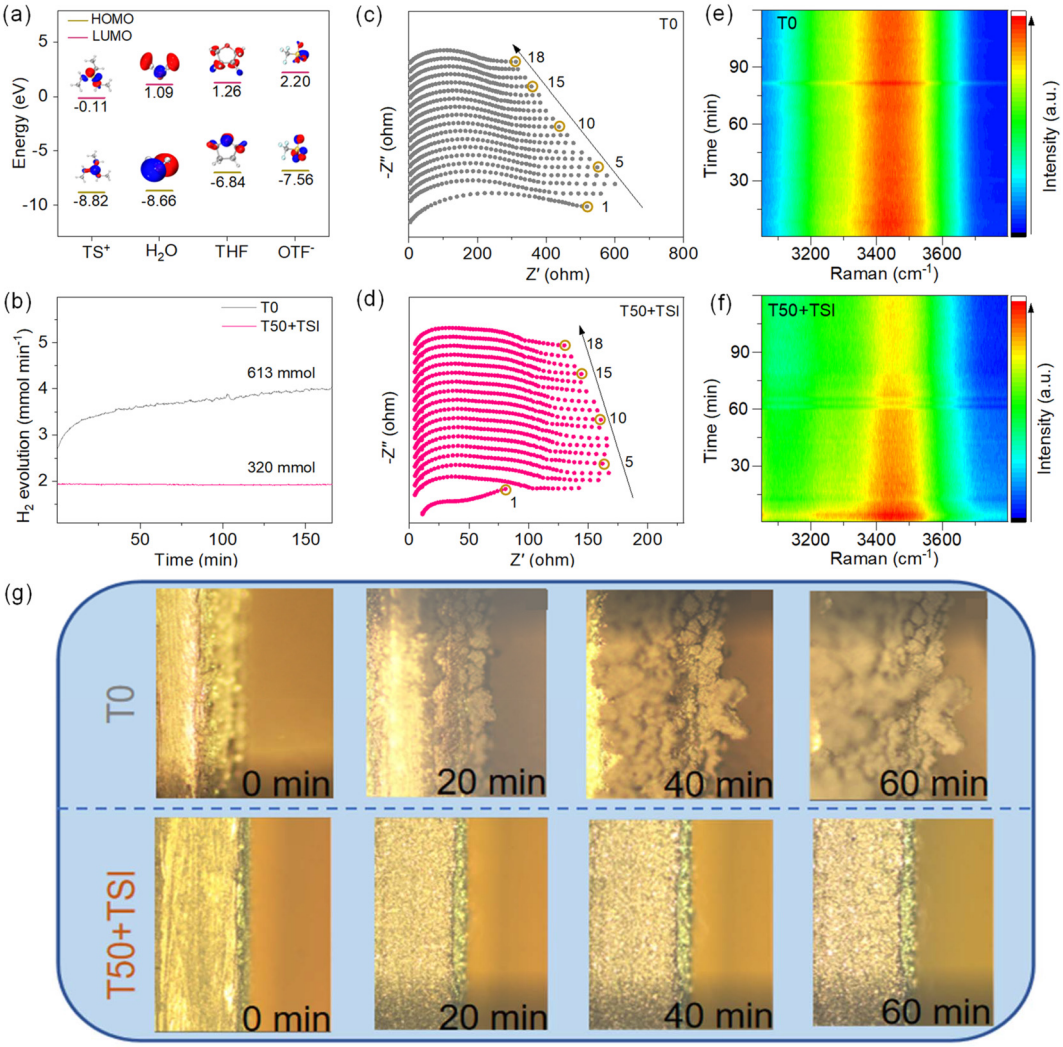


**Fig. 3** Analysis and characterization of Zn anodes working in T0 or T50 + TSI. (a) The HOMO and LUMO of several components in T50 + TSI. (b) *In situ* DEMS monitoring of the hydrogen evolution of the Zn//Zn cells using T0 or T50 + TSI at a current of 5 mA $cm^{-2}$. (c and d) *In situ* EIS data of the Zn//Zn symmetric cells during the discharge process with (c) T0 or (d) T50 + TSI. (e and f) *In situ* Raman test of the symmetric cells during the Zn plating/stripping process with (e) T0 or (f) T50 + TSI. (g) *In situ* optical microscopy images of the Zn electrodes in T0 and T50 + TSI during the Zn plating process at a current of 5 mA $cm^{-2}$.

$TS^+$, and THF reconstructs the surface of the Zn anode, further suppressing the occurrence of HER and corrosion. The adsorption of $I^-$ and $TS^+$ reconstructs the electric double layer (EDL), with $I^-$ establishing strong electrostatic adsorption to $Zn^{2+}$ on the Zn surface, guiding the Zn deposition through electrostatic interactions and modulating the growth morphology of the deposited Zn. More importantly, the space effect and electrostatic shielding effect of $TS^+$ dendritic structures prevent water molecules from coming in contact with Zn, thus avoiding HER reactions and corrosion on the Zn anode surface.[10,44]

### Electrochemical performances of Zn electrodes in T0 or T50 + TSI

The cycling stability experiments in the Zn//Zn symmetric cells further validate the optimized hybrid electrolyte for Zn anode protection. As illustrated in Fig. 4a, the Zn//Zn symmetric cell employing T50 + TSI achieves an extended cycling lifespan exceeding 7100 hours under the testing conditions of 2 mA $cm^{-2}$/2 mAh $cm^{-2}$, with a cumulative plating capacity of 7.1 Ah $cm^{-2}$ and a consistently low polarization voltage of 92 mV. Notably, this plating capacity is significantly higher than those of co-solvent-based electrolytes documented in Fig. 4b and Table S2. In stark contrast, the control cell assembled with T0 suffers from short-circuit failure after only 160 hours under identical testing conditions. This demonstrates that T50 + TSI not only sustains the long lifespan of the batteries but also reduces polarization. The discharge/charge profiles of the symmetric batteries using T0 or T50 + TSI are also evaluated at different currents and capacities under room temperature (Fig. 4c). Although the discharge/charge overpotentials of the

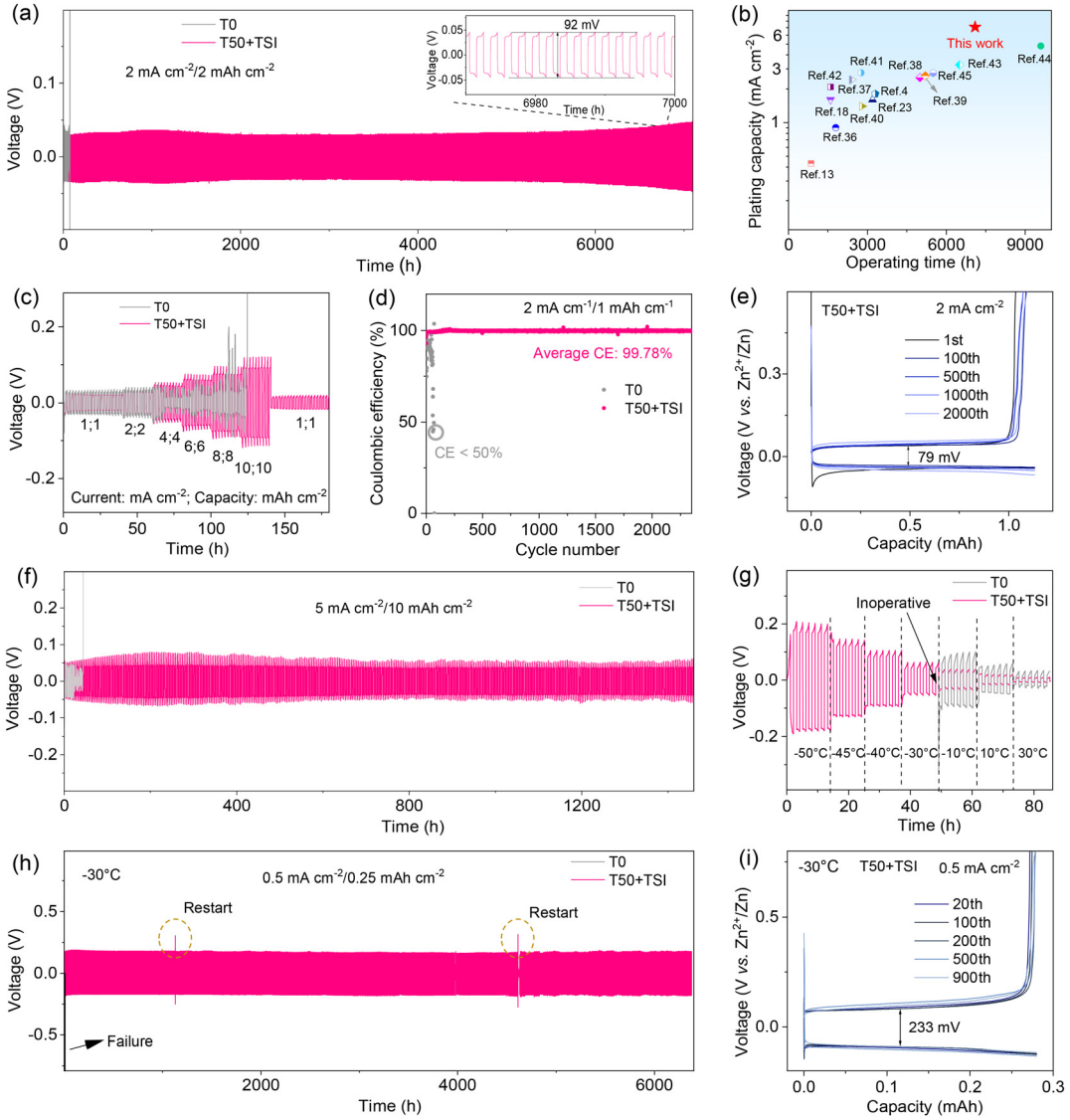


**Fig. 4** Electrochemical performances of Zn electrodes in T0 or T50 + TSI. (a) Cycling performances of the Zn//Zn cells using T0 or T50 + TSI at 2 mA $cm^{-2}$ with a limited capacity of 2 mAh $cm^{-2}$. (b) Performance comparison of the T50 + TSI-based Zn//Zn cell against literature reports. (c) Rate performances of the Zn//Zn cell using T0 or T50 + TSI at different currents. (d) CEs of the Zn//Ti cells at 2 mA $cm^{-2}$ using T0 or T50 + TSI and (e) the corresponding voltage profiles of the Zn//Ti cells using T50 + TSI. (f) Cycling performances of the Zn//Zn cells with T0 or T50 + TSI at 5 mA $cm^{-2}$/10 mAh $cm^{-2}$. (g) Discharge/charge profiles of the Zn//Zn cells in T0 or T50 + TSI under different temperatures and at 0.1 mA $cm^{-2}$ with a fixed capacity of 0.1 mAh $cm^{-2}$. (h) Long-term cycling performances of the Zn//Zn cells using T50 + TSI or T0 at −30 °C with 0.5 mA $cm^{-2}$/0.25 mAh $cm^{-2}$. (i) Voltage curves for the corresponding CE of the Zn//Ti cell with T50 + TSI at −30 °C and 0.5 mA $cm^{-2}$.

T50 + TSI based battery rise with the increase of currents and capacities, the cell maintains a stable discharge/charge profile even at a high current of 10 mA $cm^{-2}$ with a limited capacity of 10 mAh $cm^{-2}$. However, the cell using T0 exhibits an obvious short circuit phenomenon only when the current increases to 4 mA $cm^{-2}$. In addition, the Zn//Ti cells are assembled to further investigate the effects of different electrolytes on their CEs (Fig. 4d). The CE of the Zn//Ti cell with T0 begins to fluctuate severely and drops below 50% abruptly only after 70 cycles. In contrast, the Zn//Ti cell using T50 + TSI maintains good reversibility over 2300 cycles with an average CE of above 99.78%. The voltage–capacity curves shown in Fig. S13 illustrate that the Zn//Ti cell with T0 shows an average polarization voltage of 98 mV. In contrast, the Zn//Ti cell containing T50 + TSI exhibits a polarization voltage of only 79 mV (Fig. 4e). Even at a high current density of 5 mA $cm^{-2}$ and a high areal capacity of 10 mAh $cm^{-2}$ (Fig. 4f), the T0-based Zn//Zn symmetric cells can only operate for 43 hours, while the T50 + TSI-based cell significantly extends the cycle life to 1460 hours (over 2 months). More interestingly, when the depth-of-discharge of the Zn//Zn symmetric cells increases to 60% (Fig. S14), the T0-based cells only operate for 6 hours before

failure, whereas the T50 + TSI-based battery stably operates for over 260 hours. Even at a remarkably high depth of discharge (DOD) of 80%, the Zn//Zn symmetric cell with T50 + TSI maintains stable operation for 130 hours without failure.

In order to assess the utility of T50 + TSI in harsh environments, Fig. 4g presents the discharge/charge profiles of the Zn//Zn cells employing T0 or T50 + TSI at various temperatures. Remarkably, the T50 + TSI-based Zn//Zn cell still retains stable voltage curves even at an ultra-low temperature of −50 °C, with average overpotentials of <0.2 V. In contrast, the T0-containing cell cannot normally work below −10 °C. These demonstrate the superior low-temperature adaptability of the T50 + TSI system. In addition, the Zn//Zn battery with T50 + TSI exhibits the long-term cycling stability of 6400 hours at −30 °C (Fig. 4h), which is much better than the T0-based cell (<1 hour) and many of the reported co-solvent based batteries (Table S3). The two distinct fluctuations and discontinuities observed in Fig. 4h are attributed to the restarting of the cycling test when there is a sudden power outage. Moreover, the T50 + TSI based Zn//Ti cell presents a high CE retention of 99.4% over 980 cycles at −30 °C (Fig. S15). The voltage–capacity curves depicted in Fig. 4i reveal that the average polarization voltage of the Zn//Ti battery with T50 + TSI is only 233 mV at −30 °C. The good high-temperature stability is further evidenced by the Zn//Zn symmetric cell tests at 60 °C (Fig. S16). The T50 + TSI-based cell enables stable operation exceeding 180 h, in sharp contrast to the rapid failure (within 10 h) observed in the T0-based cell. These results confirm that the synergistic effect of TSI and THF effectively improves the electrochemical performances of the T50 + TSI-based batteries even under extreme environments.

### Characterization of the cycled Zn anode interfaces

To explore the underlying reasons for the stable operation of T50 + TSI, X-ray diffraction (XRD) patterns of the cycled Zn anodes in the Zn//Zn batteries assembled with T0 or T50 + TSI at 2 mA $cm^{-2}$ with an areal capacity of 2 mAh $cm^{-2}$ after 50 cycles are studied (Fig. 5a). As shown in Fig. 5a, there are several obvious peaks assigned to by-products (basic zinc salts ($Zn_xOTF_y(OH)_{2x-y}{\cdot}nH_2O$)) at the cycled Zn anode in the T0-based battery, but not at the cycled Zn anode in the T50 + TSI system, which suggests that T50 + TSI can inhibit side reactions. Moreover, the intensity ratio of (002)/(101) assigned to metallic Zn for the cycled anode in the T0 system is only 0.38. In comparison, the strength ratio of (002)/(101) for the cycled anode in the T50 + TSI system increases to 0.99. This indicates that T50 + TSI facilitates the deposition of metallic Zn along the (002) crystallographic plane, which is beneficial for inhibit-

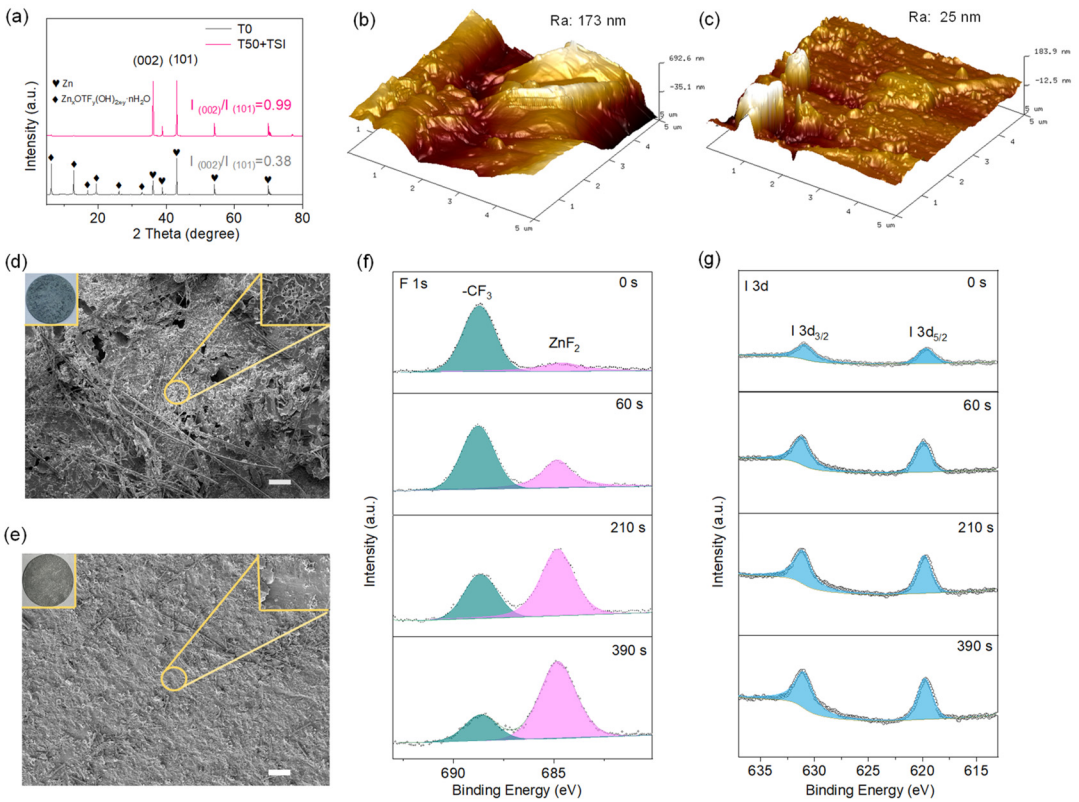


**Fig. 5** Characterization of the interfaces for the cycled Zn anodes in T0 or T50 + TSI. (a) XRD patterns of the cycled Zn anodes in T0 or T50 + TSI. (b and c) AFM images of the cycled Zn anodes in (b) T0 or (c) T50 + TSI systems. (d and e) Digital photographs (insert) and the corresponding SEM images of the cycled Zn anodes in (d) T0 and (e) T50 + TSI systems (scale bar, 10 μm). (f and g) XPS spectra at different etching depths of the cycled Zn anode in the T50 + TSI system: (f) F 1s spectra and (g) I 3d spectra.

ing side reactions.[45] Atomic force microscopy (AFM) tests are also conducted to obtain the surface roughness of the cycled Zn anodes in T0 or T50 + TSI. It can be seen from Fig. 5b and c that the average surface roughnesses of zinc sheets cycled after 50 cycles in T0 and T50 + TSI are 173 and 25 nm, respectively, further confirming that T50 + TSI can promote uniform Zn deposition on anodes. In addition, the cycled Zn anode in the symmetrical cell fabricated with T0 exhibits a significant rough surface and some of the Zn-based deposits are even grown on the separator after 50 cycles, while the cycled Zn anode in the cell with T50 + TSI maintains the smooth surface and no obvious Zn-based settlings are observed on the separator (Fig. S17). The surface photos and SEM images of the cycled Zn anodes in T0 or T50 + TSI systems are also studied (Fig. 5d and e). Obviously, there are many dendrites and corrosion holes on the cycled Zn anode in T0 (Fig. 5d). In contrast, uniform Zn deposition and no corrosion holes occur on the surface of the Zn anode cycled in T50 + TSI (Fig. 5e). Moreover, *in situ* EIS data of the Zn//Zn batteries using T50 + TSI or T0 over cycles are also studied (Fig. S18). It can be observed from Fig. S18 that the impedances of the cell exhibit significant fluctuations during cycling in the T0 system, suggesting that the dendritic and passivated Zn formed on anodes negatively affect the $Zn^{2+}$ transfer and reversible Zn deposition/dissolution behavior. For the T50 + TSI based cell, the EIS data show a change over the initial cycle but remain almost unchanged during the subsequent cycles. This suggests that a highly reversible process can be achieved in the T50 + TSI system, thereby enabling the long-term cycling performance.

X-ray photoelectron spectroscopy (XPS) tests are further employed to deeply analyze the SEI layer of the cycled Zn anodes in T50 + TSI (Fig. 5f and g). As shown in Fig. 5f, the F 1s peaks of T50 + TSI are deconvoluted into organic $-CF_3$ (688.6 eV) and inorganic $ZnF_2$ (684.8 eV) sub-peaks. The surface of the SEI layer for the cycled Zn anode in the T50 + TSI system is predominantly composed of organic $-CF_3$, and the content of the $-CF_3$ species gradually decreases with an increase in etching time. At the same time, the intensity of the inorganic $ZnF_2$ peak for the cycled Zn anode in the T50 + TSI system gradually increases as the etching depth increases. It is well-known that $ZnF_2$ is an excellent ion/electron conductor and exhibits outstanding corrosion resistance.[17,46] In the I 3d XPS spectra (Fig. 5g), the intensity of the I 3d peak of the Zn anode from the symmetrical cells with T50 + TSI after 50 cycles increases as the etching time increases. It is well-known that $I^-$ ions have strong electronegativity, which endows them with strong affinity for $Zn^{2+}$, thereby effectively reducing the desolvation energy barrier of zinc ions. The organic–inorganic composite SEI layer interface is formed on the Zn anode, in which the organic component-dominant outer layer exhibits excellent hydrophobicity and adaptability to volume changes, while the inorganic F component-dominant inner layer is beneficial for uniform Zn deposition.[47,48] As a result, the Zn anodes in the T50 + TSI system exhibit superior long-term cycling performance.

### Zn//NVO full battery performances in T0 or T50 + TSI

In order to evaluate the efficacy of the optimized hybrid electrolyte, we constructed ZMBs using sodium vanadate hydrate ($NaV_3O_8{\cdot}1.5H_2O$, NVO) as the cathode, a metallic Zn film as the anode and T0 or T50 + TSI as the electrolyte. The cycling stability of the Zn//NVO cells is tested at 1 A $g^{-1}$. As illustrated in Fig. 6a, the T50 + TSI based cell exhibits a high capacity of 140.0 mAh $g^{-1}$ even after 1500 cycles, with a good capacity retention rate of 79%. Nevertheless, the T0-based cell only shows a very low capacity of 8.4 mAh $g^{-1}$ after 1500 cycles. Moreover, even at a high current density of 4 A $g^{-1}$, the T50 + TSI-based cell maintains a substantial capacity of 93.2 mAh $g^{-1}$ after 1500 cycles (Fig. S19). Furthermore, in Fig. 6b, all the discharge capacities of the T50 + TSI-based full battery at the currents varying from 0.1 to 4 A $g^{-1}$ (especially at high current densities of above 1 A $g^{-1}$) are always much better than those of the T0-based full battery, indicating the good rate performances of the T50 + TSI system. Even at a high mass loading of 15.3 mg $cm^{-2}$, the NVO cathode in T50 + TSI still achieves a commendable capacity of 178 mAh $g^{-1}$ at a high current density of 0.5 A $g^{-1}$, which is close to that of the low mass-loading (4.3 mg $cm^{-2}$) NVO cathode (Fig. 6c). In addition, the charge/discharge profiles of the 15.3 mg $cm^{-2}$ NVO cathode are also similar to those of the 4.3 mg $cm^{-2}$ NVO cathode at different currents in the T50 + TSI system (Fig. 6d and S20). The capacity retention of the NVO cathode with a high-mass loading of 11.7 mg $cm^{-2}$ in T50 + TSI exceeds 227.8 mAh $g^{-1}$ at 0.1 A $g^{-1}$ after 170 cycles (Fig. S21). These results highlight the robust electrochemical kinetics of the high mass-loading NVO cathode in T50 + TSI. Moreover, the charge–discharge performances of the T50 + TSI-based Zn//NVO batteries are analyzed at various temperatures (Fig. 6e). It can be seen from Fig. 6e that the discharge capacities of the full battery at 30 °C, 10 °C, −10 °C, −30 °C, −40 °C and −50 °C are 307.9, 210.7, 129.3, 94.5, 59.5 mAh $g^{-1}$ and 22.5 mAh $g^{-1}$, respectively. This indicates that T50 + TSI can normally operate at extremely low temperatures. The T50 + TSI-based Zn//NVO cell displays a high capacity of 70.6 mAh $g^{-1}$ at 0.1 A $g^{-1}$ during the initial cycle and its capacity retention rate is as high as 79% even after 1480 cycles at −30 °C (Fig. 6f), which is much better than most of the recently reported full batteries with hybrid electrolytes under low-temperature conditions (Table S4). These demonstrate the remarkable cycling stability of the T50 + TSI system at the extra-low temperature. Furthermore, at an elevated temperature of 60 °C, the cell with T50 + TSI exhibits significantly enhanced cycling stability and a high capacity of 126.8 mAh $g^{-1}$ after 460 cycles, far exceeding the performance of the T0-based cell (Fig. S22). The T50 + TSI systems can function well in a wide range of temperatures, which can be attributed to the reconfiguration of the hydrogen bonding network by THF and the synergistic effects of $TS^+$ and $I^-$ ions. Zn//NVO pouch batteries using T50 + TSI have been successfully developed. They exhibit a high initial discharge capacity of 277.4 mAh $g^{-1}$ during the first cycle and even work stably for 150 cycles (Fig. 6g and S23). Notably, the pouch battery using

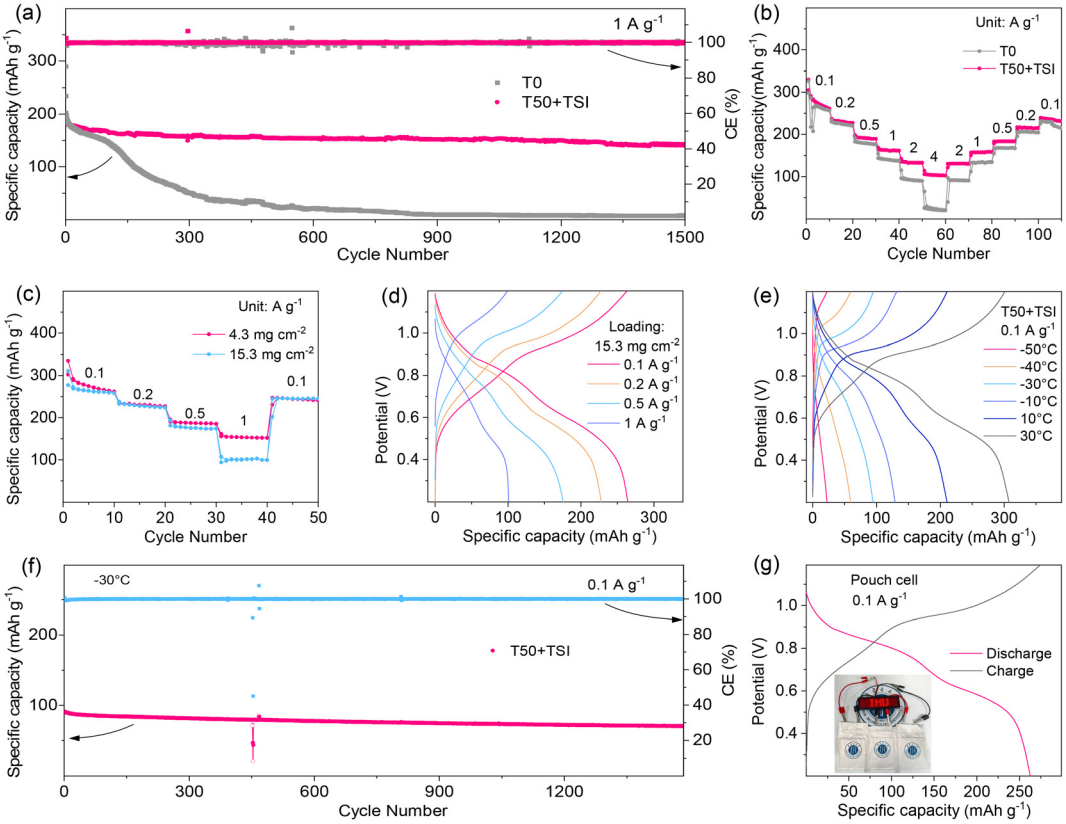


**Fig. 6** Zn//NVO full battery performances in T0 or T50 + TSI. (a) Long-term cycling performances of the Zn//NVO batteries using T0 or T50 + TSI at 1 A $g^{-1}$. (b) Rate performances of the Zn//NVO batteries using T0 or T50 + TSI. (c) The performance comparison of the NVO cathodes with high or low mass loadings in the T50 + TSI system at different current densities. (d) Galvanostatic charge/discharge profiles of the NVO cathodes with high mass loadings at different current densities. (e) Voltage profiles of the Zn//NVO full battery using T50 + TSI under different temperatures and at a current density of 0.1 A $g^{-1}$. (f) Cycling properties of the Zn//NVO full battery at 0.1 A $g^{-1}$ and −30 °C. (g) The initial galvanostatic charge/discharge profiles of the Zn//NVO pouch cell at a current density of 0.1 A $g^{-1}$ (inset: digital photograph of a Zn//NVO pouch cell powering an LED display screen).

T50 + TSI with a higher mass-loading cathode achieves an energy density of 32.5 Wh $kg^{-1}$ based on the total weight (4.2 g) of the cathode, anode and electrolyte (Fig. S24). Interestingly, the Zn//NVO pouch batteries using T50 + TSI are also capable of continuously powering the LED display board (Fig. 6g), which indicates the potential application value of T50 + TSI.

## Conclusions

In conclusion, a typical THF/$H_2O$ hybrid electrolyte with a TSI additive is prepared and further employed for ZMBs. The introduction of THF solvent reconfigures the pristine hydrogen bonding networks between $H_2O$ molecules and adjusts the solvated $Zn^{2+}$ structure, while TSI additives lower the energy barrier of $Zn^{2+}$ desolvation and optimize the interfacial layer composite between Zn anodes and hybrid electrolytes, which effectively inhibits the HER and Zn corrosion/dendritic growth and also lowers the freezing point of T50 + TSI and the Zn plating/stripping polarization on anodes. Additionally, the theoretical calculations and experimental results substantiate that T50 + TSI greatly enhances the interfacial stability of Zn anodes and also improves the operating temperature range of ZMBs. Consequently, the symmetric cell using T50 + TSI exhibits a small polarization voltage of merely 92 mV at 2 mA $cm^{-2}$ for more than 7100 hours under ambient conditions, which is much better than T0-based cells. At an extremely low temperature of −50 °C, the symmetric batteries with T50 + TSI can still work normally. The Zn//Zn battery also stably runs for >6400 hours even at −30 °C, indicating the excellent cycling stability of the T50 + TSI system under extreme temperature conditions. Moreover, the assembled Zn//NVO full batteries using T50 + TSI present a very high capacity retention rate of 79% over 1500 cycles at 1 A $g^{-1}$ and good rate performances (>100 mAh $g^{-1}$ at a high current of 4 A $g^{-1}$). Even when the mass loading of the NVO cathodes greatly increases to 15.3 mg $cm^{-2}$, the T50 + TSI-based Zn//NVO full battery still displays a high capacity of 264.0 mAh $g^{-1}$ at 0.1 A $g^{-1}$. More importantly, the Zn//NVO full battery with T50 + TSI displays amazing cycling stability for more than 1480 cycles at a very low temperature of −30 °C. This study presents that the construction of high-performance hybrid electrolytes with functional additives is very important for advanced wide-temperature ZMBs.

## Author contributions

X. Miao analyzed the experimental data and wrote the manuscript. J. Bao and C. He carried out the experiments and helped to portray the figures. S. Li performed the theoretical calculations. Z. Guo conceived the idea and designed the experiment. Y. Wang supervised the project. All the authors commented on the manuscript and approved it for publication.

## Conflicts of interest

There are no conflicts to declare.

## Data availability

The Supplementary Information (SI) provides detailed experimental procedures, characterization instruments and equipment, elaborate theoretical calculation methodologies, FT-IR spectra, Raman spectra, Photograph, EIS spectra, contact-angle measurements, and the electrochemical performances of the various samples. See DOI: https://doi.org/10.1039/d5eb00158g.

## Acknowledgements

This work was supported by the National Natural Science Foundation of China (22379074 and U24A20565), the National Key R&D Program of China (2024YFE0101100), the Natural Science Foundation of Inner Mongolia (2024JQ07) and the Young Science and Technology Talent Program of Inner Mongolia Province (NJYT24001).

## References

1 Y. Liu, X. Lu, F. Lai, T. Liu, P. R. Shearing, I. P. Parkin and G. He, *Joule*, 2021, **5**, 2845–2903.
2 H. Pan, Y. Shao, P. Yan, Y. Cheng, K. S. Han, Z. Nie, C. Wang, J. Yang, X. Li, P. Bhattacharya, K. T. Mueller and J. Liu, *Nat. Energy*, 2016, **1**, 16039.
3 L. Zhang, J. Xiao, X. Xiao, W. Xin, Y. Geng, Z. Yan and Z. Zhu, *eScience*, 2024, **14**, 100205.
4 Z. Li, Y. Liao, Y. Wang, J. Cong, H. Ji, Z. Huang and Y. Huang, *Energy Storage Mater.*, 2023, **56**, 174–182.
5 L. Yuan, J. Hao, B. Johannessen, C. Ye, F. Yang, C. Wu, S.-X. Dou, H.-K. Liu and S.-Z. Qiao, *eScience*, 2023, **3**, 100096.
6 D. Kundu, S. Hosseini Vajargah, L. Wan, B. Adams, D. Prendergast and L. F. Nazar, *Energy Environ. Sci.*, 2018, **11**, 881–892.
7 W. Yang, X. Du, J. Zhao, Z. Chen, J. Li, J. Xie, Y. Zhang, Z. Cui, Q. Kong, Z. Zhao, C. Wang, Q. Zhang and G. Cui, *Joule*, 2020, **4**, 1557–1574.
8 H. Geng, M. Cheng, B. Wang, Y. Yang, Y. Zhang and C. C. Li, *Adv. Funct. Mater.*, 2020, **30**, 1907684.
9 X. Lu, Z. Liu, A. Amardeep, Z. Wu, L. Tao, K. Qu, H. Sun, Y. Liu and J. Liu, *Angew. Chem., Int. Ed.*, 2023, **62**, e202307475.
10 M. Li, X. Wang, J. Hu, J. Zhu, C. Niu, H. Zhang, C. Li, B. Wu, C. Han and L. Mai, *Angew. Chem.*, 2023, **135**, e202215552.
11 J. Ren, H. Yan, X. Xu, S. Li and B. Li, *Chem. Eng. J.*, 2024, **498**, 155257.
12 J. Yao, B. Zhang, X. Wang, L. Tao, J. Ji, Z. Wu, X. Liu, J. Li, Y. Gan, J. Zheng, L. Lv, X. Ji, H. Wang, J. Zhang, H. Wang and H. Wan, *Angew. Chem., Int. Ed.*, 2024, **63**, e202409986.
13 Z. Chen, T. Shen, M. Zhang, X. Xiao, H. Wang, Q. Lu, Y. Luo, Z. Jin and C. Li, *Adv. Funct. Mater.*, 2024, **3**, 2314864.
14 J. Wan, R. Wang, Z. Liu, S. Zhang, J. Hao, J. Mao, H. Li, D. Chao, L. Zhang and C. Zhang, *Adv. Mater.*, 2023, **36**, 2310623.
15 C. You, R. Wu, X. Yuan, L. Liu, J. Ye, L. Fu, P. Han and Y. Wu, *Energy Environ. Sci.*, 2023, **16**, 5096–5107.
16 D. Feng, F. Cao, L. Hou, T. Li, Y. Jiao and P. Wu, *Small*, 2021, **17**, 2103195.
17 J. Liu, C. Yang, X. Chi, B. Wen, W. Wang and Y. Liu, *Adv. Funct. Mater.*, 2021, **32**, 2106811.
18 A. Wang, W. Zhou, A. Huang, M. Chen, Q. Tian and J. Chen, *J. Colloid Interface Sci.*, 2021, **586**, 362–370.
19 M. M. Gross and A. Manthiram, *Energy Storage Mater.*, 2019, **19**, 346–351.
20 F. Ming, Y. Zhu, G. Huang, A.-H. Emwas, H. Liang, Y. Cui and H. N. Alshareef, *J. Am. Chem. Soc.*, 2022, **144**, 7160–7170.
21 Z. Hou, Z. Lu, Q. Chen and B. Zhang, *Energy Storage Mater.*, 2021, **42**, 517–525.
22 Q. Li, K. K. Abdalla, J. Xiong, Z. Song, Y. Wang, Y. Zhao, M. Liu, Y. Fan, Y. Zhao and X.-M. Sun, *Energy Mater.*, 2024, **4**, 400040.
23 P. Xiong, Y. Kang, N. Yao, X. Chen, H. Mao, W. Jang, D. Halat, Z. Fu, M. Jung, H. Y. Jeong, Y. Kim, J. A. Reimer, Q. Zhang and H. S. Park, *ACS Energy Lett.*, 2023, **8**, 1613–1625.
24 M. Xu, B. Zhang, Y. Sang, D. Luo, R. Gao, Q. Ma, H. Dou and Z. Chen, *Energy Environ. Sci.*, 2024, **17**, 8966–8977.
25 Q. Li, D. Luo, Q. Ma, Z. Zheng, S. Li, Y. Xie, L. Xue, M. Lin, Y. Nie, G. Feng, H. Dou, J. Chen, X. Wang and Z. Chen, *Energy Environ. Sci.*, 2025, **18**, 1489–1501.
26 Y. Wang, Z. Wang, W. K. Pang, W. Lie, J. A. Yuwono, G. Liang, S. Liu, A. M. D'Angelo, J. Deng, Y. Fan, K. Davey, B. Li and Z. Guo, *Nat. Commun.*, 2023, **14**, 2720.
27 H. Jia, X. Jiang, Y. Wang, Y. Lam, S. Shi and G. Liu, *Adv. Energy Mater.*, 2024, **14**, 2304285.
28 Y. Xie, J. Wang, B. H. Savitzky, Z. Chen, Y. Wang, S. Betzler, K. Bustillo, K. Persson, Y. Cui, L. Wang, C. Ophus, P. Ercius and H. Zheng, *Sci. Adv.*, 2023, **9**, eadc9721.
29 H. Wang, W. Ye, B. Yin, K. Wang, M. S. Riaz, B. Xie, Y. Zhong and Y. Hu, *Angew. Chem., Int. Ed.*, 2023, **62**, e202218872.

30 M. Qiu, P. Sun, A. Qin, G. Cui and W. Mai, *Energy Storage Mater.*, 2022, **49**, 463–470.
31 H. Du, Y. Dong, Q. Li, R. Zhao, X. Qi, W. Kan, L. Suo, L. Qie, J. Li and Y. Huang, *Adv. Mater.*, 2023, **35**, 2210055.
32 W. Yuan, X. Nie, G. Ma, M. Liu, Y. Wang, S. Shen and N. Zhang, *Angew. Chem., Int. Ed.*, 2023, **62**, e202218386.
33 F. Bu, Y. Gao, W. Zhao, Q. Cao, Y. Deng, J. Chen, J. Pu, J. Yang, Y. Wang, N. Yang, T. Meng, X. Liu and C. Guan, *Angew. Chem., Int. Ed.*, 2024, **63**, e202318496.
34 G. Guo, C. Ji, J. Lin, T. Wu, Y. Luo, C. Sun, M. Li, H. Mi, L. Sun and H. J. Seifert, *Angew. Chem., Int. Ed.*, 2024, **63**, e202407417.
35 J. Ruan, D. Ma, K. Ouyang, S. Shen, M. Yang, Y. Wang, J. Zhao, H. Mi and P. Zhang, *Nano-Micro Lett.*, 2023, **15**, 37.
36 B. Niu, Z. Li, D. Luo, X. Ma, Q. Yang, Y.-E. Liu, X. Yu, X. He, Y. Qiao and X. Wang, *Energy Environ. Sci.*, 2023, **16**, 1662–1675.
37 Q. Deng, S. You, W. Min, Y. Xu, W. Lin, J. Lu and C. Yang, *Adv. Mater.*, 2024, **36**, 2312924.
38 J. Luo, L. Xu, Y. Zhou, T. Yan, Y. Shao, D. Yang, L. Zhang, Z. Xia, T. Wang, L. Zhang, T. Cheng and Y. Shao, *Angew. Chem., Int. Ed.*, 2023, **62**, e202302302.
39 L. Miao, R. Wang, S. Di, Z. Qian, L. Zhang, W. Xin, M. Liu, Z. Zhu, S. Chu, Y. Du and N. Zhang, *ACS Nano*, 2022, **16**, 9667–9678.
40 P. Wang, Y. Zhong, J. Wang, H. Zhou, G. Sun, X. Sui and Z. Wang, *Adv. Funct. Mater.*, 2024, **35**, 2414563.
41 Y. Liu, M. Qiu, Y. Liang, J. Zhang, J. Chen, P. Sun and W. Mai, *Angew. Chem., Int. Ed.*, 2025, **64**, e202506010.
42 J. Cong, Z. Hu, L. Hu, T. Li, H. Ji, Z. Long, Y. Fan, Z. Wen, Y.-C. Lin, H. Xu, Z. Li, S. Li, F. Pan and Y. Huang, *Adv. Funct. Mater.*, 2025, **35**, 2424423.
43 Z. Huang, Z. Li, Y. Wang, J. Cong, X. Wu, X. Song, Y. Ma, H. Xiang and Y. Huang, *ACS Energy Lett.*, 2023, **8**, 372–380.
44 S. You, Q. Deng, Z. Wang, Y. Chu, Y. Xu, J. Lu and C. Yang, *Adv. Mater.*, 2024, **36**, 2402245.
45 J. Heo, D. Dong, Z. Wang, F. Chen and C. Wang, *Joule*, 2025, **9**, 101844.
46 M. Wang, J. Ma, Y. Meng, J. Sun, Y. Yuan, M. Chuai, N. Chen, Y. Xu, X. Zheng, Z. Li and W. Chen, *Angew. Chem., Int. Ed.*, 2022, **62**, 202214966.
47 D. Dong, T. Wang, Y. Sun, J. Fan and Y. Lu, *Nat. Sustainability*, 2023, **6**, 1474–1484.
48 D. Li, L. Cao, T. Deng, S. Liu and C. Wang, *Angew. Chem., Int. Ed.*, 2021, **60**, 13035–13041.